Ejecta velocities in twice-shocked liquid metals under extreme conditions: A hydrodynamic approach

View Online   Export Citation   CrossMark

V. Karkhanis [iD] and P. Ramaprabhu [iD]

AFFILIATIONS

University of North Carolina, Charlotte, North Carolina 28223-0001, USA

ABSTRACT

We apply a hydrodynamic approach to analyze ejecta emanating from doubly shocked liquid metals. In particular, we are interested in characterizing ejecta velocities in such situations by treating the problem as a limiting case of the Richtmyer–Meshkov instability. We find existing models for ejecta velocities do not adequately capture all the relevant physics, including compressibility, nonlinearities, and nonstandard shapes. We propose an empirical model that is capable of describing ejecta behavior across the entire parameter range of interest. We then suggest a protocol to apply this model when the donor material is shocked twice in rapid succession. Finally, the model and the suggested approach are validated using detailed continuum hydrodynamic simulations. The results provide a baseline understanding of the hydrodynamic aspects of ejecta, which can then be used to interpret experimental data from target experiments.

I. INTRODUCTION

Ejecta are typically formed at the free surface of a target metal when it is loaded by explosives, ballistic plate impact, or a laser source. The dynamics of material transport resulting from particle ejections at the metallic free surface are of great interest in high-energy-density applications.[1–4] The problem of mass ejections from shocked free surfaces is complex and involves multiple physical phenomena, yet it has been shown that significant progress can be made by treating the ejection process as a limiting case of the Richtmyer–Meshkov (RM) instability.[5,6] In recent years, this approach has been successfully employed in developing models for the mass source,[7,8] extension to nonstandard shapes,[7,9] predicting the velocities of the bubble cavities,[10] developing self-similar models of ejecta growth,[11,12] and even using ejecta hydrodynamics to diagnose the yield strength of a material.[13,14] The objective of this paper is to build on this progress to (i) propose an empirical model for ejecta velocities, (ii) suggest an approach to apply the model to doubly shocked metals, and (iii) validate these ideas using high-fidelity, continuum numerical simulations. By focusing solely on the hydrodynamic aspects, we have avoided complicating factors such as material defects, spallation, and uncertainties in the equations of state.

There has been significant recent interest in the ejecta problem, encompassing theory,[7–13,15,16] simulations,[7,13,16–22] and experiments.[13–15,23–27] For recent detailed reviews, we refer the reader to Refs. 28 and 29. In contrast, there have been few detailed studies of the corresponding double-shock problem. Charakhch'an[30] performed numerical simulations of doubly shocked ejecta in Al, which had been rendered in a liquid state following the strong shocks. Continuum simulations of doubly shocked Pb samples were investigated in Ref. 19 for initial perturbation properties matching machined grooves on coupons used in experiments. In Ref. 31, we extended a recently proposed ejecta source model to the multiply shocked situation, and validated the approach using continuum simulations. Researchers from Los Alamos National Laboratory (LANL) reported measurements using a novel two-shockwave tool[24,25] that was used to study ejecta from multiple shocks emanating from an Sn target. Measurements from the experimental campaign included cumulative ejecta mass and time-resolved velocities from both shock events.

The RM instability occurs when a material interface separating different fluids is impulsively accelerated, usually by a shockwave that has just crossed the interface boundary. Thus, perturbations imposed at the interface are amplified as a result of the baroclinic vorticity deposited by the shock–interface interaction. If the fluids straddling the boundary have densities ρ_A and ρ_B, an important parameter governing the growth of the interface is the Atwood number

$$A = \frac{\rho_B - \rho_A}{\rho_B + \rho_A}.$$

Then, hydrodynamic aspects of the ejecta phenomenon may be understood by treating it as a limiting case of the RM instability, where $A \to -1$ (corresponding to the RM case where the tenuous material has a vanishing density). The resulting instability growth occurs in stages and depends on the initial interface perturbation amplitude h_0 relative to its wavenumber $k \equiv 2\pi/\lambda$. When $kh_0 \ll 1$ [or $kh(t) \ll 1$], the growth rates are obtained by linearizing the perturbation equations, and this situation is therefore referred to as *linear* growth. When either condition is violated, higher-order harmonics become significant, resulting in *nonlinear* growth of the interface. These harmonics shape the interface into distinct *bubble* cavities penetrating the heavy fluid and *spike* channels of heavy fluid advancing into the light fluid. In the ejecta limit, bubbles are rounded wells advancing into the donor material, while spikes are long and narrow jets, which are the ejecta.

In this paper, we address the issue of ejecta velocities in materials that are subjected to two shocks. The problem has gained recent relevance following the successful double-shock experimental campaign conducted at LANL[24,25] through the development of a unique two-shockwave physics package. The remainder of the paper is organized as follows. In Sec. II A, we review previous models for bubbles and spikes, and suggest an empirical model for ejecta velocities that addresses some shortcomings of earlier efforts. In Sec. II B, we discuss shape effects, and then, in Sec. II C, we suggest a protocol for applying the model to the double-shock problem by properly accounting for these effects. In Sec. III we describe the numerical methods and problem setup. The results, which include a detailed comparison of our simulation results with the model over a wide range of conditions, are presented in Sec. IV A, and we present a preliminary comparison with the experimental results of Refs. 24 and 25 in Sec. IV B. We conclude with a summary in Sec. V.

II. EJECTA MODELS

A. Bubble and spike velocity models

We briefly review previous efforts to describe linear and nonlinear growth rates associated with the RM instability and the ejecta phenomenon. A more detailed summary can be found in recent papers on this subject (see, e.g., Ref. 32). Throughout this paper, we adopt the following nomenclature to clarify the different quantities under discussion: the symbols h and V represent interface amplitudes and velocities, and the ejecta mass is denoted by m. The states of these quantities are indicated by subscripts and superscripts. Specifically, initial states are indicated by the subscript 0, while pre- and post-shock states are indicated by superscripts $-$ and $+$, respectively. However, for the states immediately preceding and following the second shock, we use the superscripts $--$ and $++$, respectively. Finally, when discussing quantities derived from theoretical models, we use the authors' initials as superscripts to identify the models.

In the ejecta limit ($A \to -1$), the linear growth rate of interfacial perturbations amplified by an incident shock with a velocity W_i is given by[5,33]

$$V_0^{MB} = F^C k h_0^- \Delta U, \tag{1}$$

where ΔU is the RM interface velocity (or free-surface velocity in the case of ejecta), and $F^C = 1 - \Delta U/2W_i$ accounts for shock compression of the groove. When the interface transitions to

nonlinear growth followed by differentiation into bubbles and spikes, Eq. (1) is no longer adequate for describing the growth rates. Mikaelian[10] used the potential flow approach (first introduced by Layzer[34] for such flows) to obtain an expression for the time-dependent bubble velocity:

$$V_{bu}^{KM}(t) = \frac{V_{bu,0}}{1 + \frac{3}{2}V_{bu,0}kt}, \tag{2}$$

where $V_{bu,0}$ represents an initial bubble velocity, which could itself be compromised by nonlinear effects when $kh_0^- > 1$. To address this effect, Buttler *et al.*[23] suggested using $V_{bu,0}^{WB} = F_{bu}^{NL}V_0^{MB}$, where F_{bu}^{NL} is a nonlinear correction factor that was obtained as a fit to higher-order expressions based on Padé approximants[35] and is given by

$$F_{bu}^{NL} = \frac{1}{1 + \frac{1}{6}kh_0^-}. \tag{3}$$

The corresponding spike model was developed by Zhang,[36] starting from potential flow theory, but taking the spike curvature as being opposite in sign to the bubble curvature: $\xi_{spike} = -\xi_{bubble} = kh_0/2$. Asymptotically, this leads to a terminal velocity for the spike tip, which is obtained from the model as

$$V_{sp}^{QZ} = V_0 \sqrt{3\frac{kh_0^- + 1}{3kh_0^- + 1}}, \tag{4}$$

where nonlinear effects arising from finite-amplitude initial conditions are encapsulated through the term under the square root. Once again, Zhang[36] did not specify a choice for the initial velocity V_0 in Eq. (4), but for $kh_0^- \geq 1$ it is expected the initial growth rate will be decreased from the ideal. Dimonte and Ramaprabhu[37] and Buttler *et al.*[23] suggest a nonlinear correction factor for the initial spike velocities (obtained as a curve fit to the more detailed expression consisting of Padé approximants given in Ref. 35),

$$F_{sp}^{NL} = \frac{1}{1 + \left(\frac{1}{2}kh_0^-\right)^2}. \tag{5}$$

Thus, the initial bubble and spike velocities in Eqs. (2) and (4) must first be computed as suggested by Buttler *et al.*[23] according to

$$V_{bu0/sp0}^{WB} = F_{bu/sp}^{NL}V_0^{MB}. \tag{6}$$

Spike growth can also be inhibited at high Mach numbers of the incident shock, M_i, as suggested by Dimonte *et al.*[16] and observed in numerical simulations.[32] Pending a fully compressible potential flow model for spikes, Dimonte *et al.*[16] proposed an empirical model for the asymptotic spike velocity that depends on M_i, kh_0, and the initial bubble velocity according to

$$V_{bu0}^{GD} = \frac{V_0^{MB}}{1 + \phi_{bu}kh_0^-}, \quad V_{sp}^{GD} = |V_{bu0}^{GD}|\sqrt{\phi_{sp}^2\frac{kh_0^- + 1}{3M_ikh_0^- + 1}}. \tag{7}$$

The suggested values for the empirical coefficients are $\phi_{bu} \sim 0.45$, and $\phi_{sp} = 3.5\gamma_A/(1 + \gamma_A)$, where γ_A is the adiabatic index of the donor metal. While Eq. (7) predicts spike velocities at finite values of M_ikh_0, it does not approach the exact incompressible model (4) in the limit of $M_ikh_0 \to 0$.

To address the shortcomings of existing models, and to explain observed ejecta velocities across a wide range of perturbation groove

amplitudes and incident shock Mach numbers, we recently proposed[32] an empirical model for the asymptotic spike velocity:

$$V_{sp} = V_{MB} \sqrt{3 \, \frac{kh_0^- + 1}{3M_i (kh_0^-)^2 + 1}}. \tag{8}$$

When expressed in the form of Eq. (8), our model has the advantage that it avoids the ambiguities associated with the calculation of the initial velocity V_{sp0}, and can instead be computed entirely in terms of well-defined quantities such as M_i and kh_0^-. When recast in the form of Eq. (4), the proposed empirical model for ejecta is expressed as

$$V_{sp} = F_{sp}^{NL} V_0^{MB} \sqrt{3 \, \frac{kh_0^- + 1}{3kh_0^- + 1}}, \tag{9}$$

where F_{sp}^{NL} can be interpreted as a prefactor that accounts for both nonlinearities in the initial conditions and compressibility, and is now given by

$$F_{sp}^{NL} = \sqrt{\frac{3kh_0^- + 1}{3M_i (kh_0^-)^2 + 1}}. \tag{10}$$

As shown in Ref. 32 and in Sec. III of the present paper, Eq. (8) accurately captures ejecta behavior due to nonlinearities and compressibility effects without the need for tunable coefficients, but reverts to the same forms as the exact incompressible, potential flow model result of Ref. 36 in the limit of $kh_0 \to 0$ or $M_i kh_0 \to 0$. For $M_i \to 1$, the models diverge for $kh_0 \gg 1$, with significant evidence from experiments and simulations that Eq. (8) more accurately explains the data reported in Refs. 15, 23, 26, and 27. Note that in Eqs. (8) and (10), compressibility effects are coupled to the nonlinear term through the incident shock Mach number, so that even at low values of M_i, these effects may be significant at large enough values of kh_0. Indeed, this is the situation encountered in several experiments that use target coupons with groove amplitudes $kh_0 \gg 1$, or in doubly shocked flows where the interface perturbation from the first shock has matured to a nonlinear amplitude prior to arrival of the second shock.

B. Shape effects

For targets with nonsinusoidal perturbation grooves, Cherne et al.[7] argued that the longest wavelength associated with the perturbation is responsible for sourcing most of the mass. In practice, this can be accounted for by defining an effective wavelength $\lambda_{eff} = A_{sh}/h_0$, where A_{sh} is the missing area under the interface profile (i.e., negative space) and h_0 is the half-amplitude. Thus, λ_{eff} can be considered the wavelength of an equivalent sinusoid that sources the same amount of mass as the profile under consideration, and when used in source models was found to accurately predict the ejecta areal mass for different shapes. The same approach can be extended to velocities, and was found to be successful in Ref. 32. Thus, the bubble velocity model of Ref. 10 can be written as

$$V_{bu}(t) = \frac{(V_{bu0}^{WB})_{eff}}{1 + t/\tau_{eff}}, \tag{11}$$

where $(V_{bu0}^{WB})_{eff}$ is the initial bubble velocity with the nonlinear correction given in Eq. (3) and evaluated using λ_{eff}. In Eq. (11), τ_{eff} represents a nonlinear time scale over which the bubble saturates, and is given by $\tau_{eff} = \lambda_{eff}/3\pi (V_{bu0}^{WB})_{eff}$. The corresponding spike

velocity from our proposed model [or alternatively Eq. (4)] can be extended to nonstandard shapes using

$$V_{sp} = \left(F_{sp}^{NL}\right)_{eff} \left(V_0^{MB}\right)_{eff} \sqrt{3 \, \frac{(kh_0^-)_{eff} + 1}{3 (kh_0^-)_{eff} + 1}}, \tag{12}$$

where terms with the subscript *eff* are computed using the effective wavelengths and wavenumbers, respectively. Equations (11) and (12) were validated using continuum hydrodynamics and molecular dynamics simulations in Ref. 32, for interfaces with sinusoidal, Gaussian, flycut, and chevron profiles.

C. Approach for doubly shocked ejecta

When an interface is subjected to multiple shocks, our hypothesis is that it is the bubble profile (amplitude and effective wavelength) at the time of arrival of each shock that explains the ejecta mass and velocity. In Ref. 31, we validated this hypothesis for ejecta mass using data from simulations and experiments, and we address the issue of velocities in the current work. The bubble surface can acquire a nonsinusoidal shape by the time of arrival of the second shock, owing to the influence of higher harmonics in the perturbation equations. Specifically, we find the nonlinear bubble most closely resembles the shape carved out by a flycutter machining tool, which we refer to as a "flycut." The equation for a flycut graph is parametrized by three independent parameters [Fig. 1(a)], namely, the bubble amplitude h_{bu} [the distance between the free surface—the dashed line in Fig. 1(a)—and the bubble apex], the wavelength of the original sinusoidal perturbation λ, and R, which is the radius of an off-center circle centered at C and osculates with the bubble surface. The flycut profile is then given by

$$h(x) = \begin{cases} h_{bu}, & 0 \le x \le \frac{1}{2}\lambda - b, \\[2mm] R - h_{bu} - \sqrt{R^2 - \left(x - \frac{1}{2}\lambda\right)^2}, & \frac{1}{2}\lambda - b < x < \frac{1}{2}\lambda + b, \\[2mm] h_{bu}, & \frac{1}{2}\lambda + b \le x < \lambda. \end{cases} \tag{13}$$

where x is the coordinate aligned with the shock direction and $b = \sqrt{R^2 - (R - 2h_{bu})^2}$ is the chord length of the circle at a distance of $2h_{bu}$ from the bubble tip [Fig. 1(a)]. We find that representing the bubble profile with a sinusoidal or parabolic waveform[31] under-counts the missing area of the perturbation and hence the subsequent ejecta areal mass. We show this in Fig. 1(b), where we compare the nonlinear bubble surface from one of our simulations with various potential waveforms. The solid vertical line represents the location of the free surface also obtained from the simulation. As shown in Fig. 1(b), a sine perturbation undercounts the missing area of the bubble and would therefore under-predict the amount of ejecta that this bubble would produce when shocked.[31]

When working with data from simulations and experiments, it is more convenient to use a lateral bubble length scale rather than R to define the flycut profile. Thus, we choose the bubble half-width L_{bu} (Fig. 1) as the positive y intercept of the bubble profile, with the free surface as the third independent parameter in defining the flycut
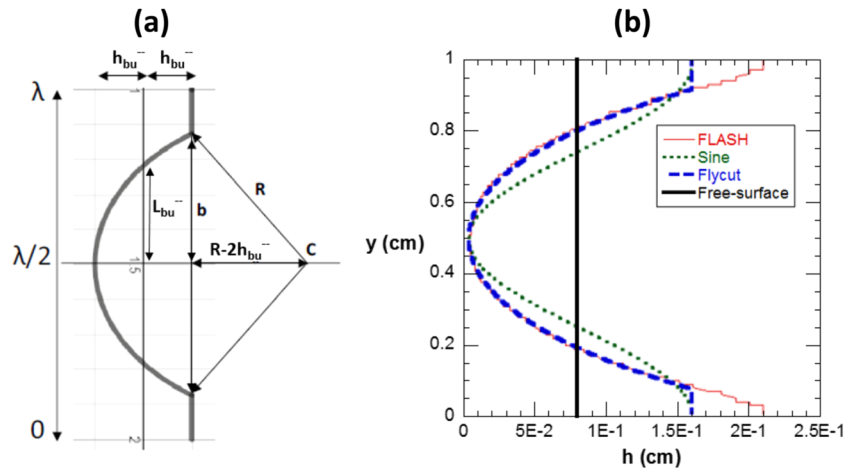
FIG. 1. (a) Geometric parameters associated with a flycut profile and (b) flycut and sine waveforms fitted to bubble surface from numerical simulations. The solid vertical line indicates the free surface.

profile. If the corresponding spike half-width is L_{sp}, then $2(L_{bu} + L_{sp}) = \lambda$. From Fig. 1(a), it is clear that

$$R = \frac{1}{2}\left(h_{bu} + \frac{L_{bu}^2}{h_{bu}}\right), \tag{14}$$

so the flycut profile may be specified instead in terms of $(h_{bu}, L_{bu}, \lambda)$. The bubble half-width is directly available from simulation data or by computing the streamlines from recently proposed similarity models[11] of ejecta (see Sec. IV B). The missing area is the area bound by the bubble tip and the flat surface [at a distance $2h_{bu}$ from the bubble tip in Figs. 1(a) and 1(b)] and is given by

$$A_{sh} = \theta R^2 - b(R - 2h_{bu}), \tag{15}$$

where $\theta = \arcsin(b/R)$. Thus, our prescription for analyzing doubly shocked ejecta is as follows: From the nonlinear bubble surface just prior to the second shock, obtain the bubble half-width L_{bu}^{--}. The radius of the osculating circle R and the corresponding chord length b are computed from Eq. (14) using L_{bu}^{--} and the pre-second-shock bubble amplitude h_{bu}^{--}. The effective perturbation wavelength λ_{eff} for use in Eqs. (11) and (12) is then computed as $\lambda_{eff} = A_{sh}/h_0$ using the missing area given in Eq. (15) and h_{bu}^{--}. Finally, we note that the above analysis is only valid for bubbles that satisfy $R > 2h_{bu}^{--}$.

In the next section, we compare bubble and spike velocities from our numerical simulations with the models given in Eqs. (2), (4), (7), and (8), but evaluated for the second-shock parameters using the effective wavelength λ_{eff} as described above. For instance, Eqs. (4) and (8) were evaluated by recasting in the form of Eq. (12) in terms of the corresponding *eff* parameters.

III. NUMERICAL SIMULATION APPROACH AND PROBLEM SETUP

We validate the above ideas through detailed numerical simulations using the continuum hydrodynamics code FLASH.[38,39] Details of the numerical methods used in FLASH are provided elsewhere,[38,39] and only a brief summary is given here. FLASH solves the governing Euler equations in conservative form, while we

use an ideal gas equation of state in our simulations. The hydrodynamics are handled through the piecewise-parabolic method (PPM).[40] Adaptive mesh refinement (AMR) strategies are used, where the allocation of mesh resources is optimized based on the gradients of pressure and density variables.

The problem setup employed in our simulations in shown in Fig. 2, with terminology adapted from Refs. 37 and 41. The numerical domain represents a computational shocktube, in which a planar incident shock initialized in fluid A traverses along the positive x-coordinate direction. A material interface separates the two fluids A and B, and supports an initial perturbation with an amplitude h_0 and wavenumber k. As the shock traverses the interface from heavy (A) to light (B) fluid, a transmitted shock and a reflected rarefaction are generated. The FLASH simulations were performed with an adaptive mesh resolution equivalent to 256 zones/λ, where λ was chosen to be 1 cm for all cases. Periodic boundary conditions were used on the domain boundaries at $y = 0$ and $y = 2\lambda$, while outflow conditions
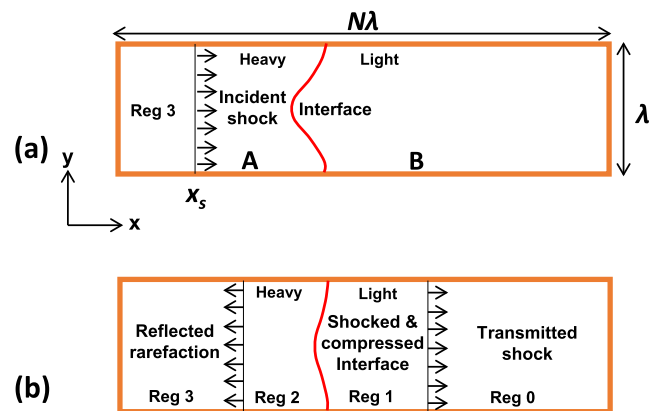

FIG. 2. Schematic showing the problem setup for FLASH simulations, with terminology from Ref. 41.

implemented on the boundaries in the shock direction ensured the egress of acoustic waves and shocks without leading to spurious oscillations within the flow region. In our simulations, we approximated the hydrodynamic response of shocked Sn by an equivalent γ-law fluid with $\rho_A = 7.3$ g/cm^3 and $\gamma_A = 3$. It has previously been shown[16] that for these conditions, the modeled γ-law fluid reproduced the U_s–U_p relationship for Sn over particle velocities ranging from 0 to 5 km/s. The light fluid (B) was chosen to have $\rho_B = 1.22 \times 10^{-3}$ g/cm^3 and $\gamma_A = 5/3$, resulting in an Atwood number $A \rightarrow -1$.

A summary of all the simulations reported in this work is given in Table I. Cases 1–5 were initialized with a sinusoidal perturbation with scaled initial amplitudes of $kh_0^- = 0.12$, while the arrival time for the second shock was varied to generate interfaces with different initial amplitudes kh_0^{--} for the second shock. Case 6 was initialized with a chevron interface with a waveform given by

$$h(y) = \frac{4h_0}{\lambda}|y| - h_0 \qquad (16)$$

and is representative of grooved perturbations on target coupons used in dynamic experiments. Table I also includes the flycut parameters associated with the pre-second-shock bubble surface, namely, the bubble half-width L_{bu}^{--}, chord length b, and effective wavelength λ_{eff}.

The x–t diagram in Fig. 3 shows the sequence of significant events captured by a typical simulation. An incident shock IS_1 with $M_i = 1.6$ is initialized in fluid A with a piston velocity, and its interaction with the material interface is labeled SI_1 in the figure. The shock–interface interaction leads to a transmitted shock TS_1 and reflected rarefaction RR_1, while the interface acquires a jump velocity ΔU^+. As the RR_1 wave leaves the domain through the x_l boundary, the guard cells adjacent to that boundary are filled with material corresponding to the conditions of a second shock IS_2. In this manner, a clean second shock can be generated, free of perturbations from the passage of exiting acoustic waves. Furthermore, the timing of the second shock (and thereby the interface amplitude prior to second shock) can be precisely controlled, enabling a systematic study of the effects of nonlinearities on the ejecta velocities. The products of the second shock interaction with the interface are labeled TS_2 and RR_2, and the jump velocity is ΔU^{++}.

IV. RESULTS AND DISCUSSION

A. Results from numerical simulations

In Figs. 4–6, we present qualitative results from our simulations by plotting the time evolution of density contours at key stages of the

flow development. The contours in Fig. 4 correspond to case 1, for a sinusoidal initial perturbation with an initial amplitude $kh_0^- = 0.12$ and a second-shock amplitude $kh_{bu}^{--} = 0.45$. The images are plotted in units of scaled time $(t - t_{SI2})/\tau^{++}$, where t_{SI2} is the time instance of second-shock arrival and τ^{++} is the bubble nondimensional time scale as defined earlier, but evaluated here for second-shock conditions. The initial configuration corresponding to a scaled time of -2.2 units is displayed in Fig. 4(a) and also shows the planar shock positioned immediately next to the sinusoidally perturbed interface. Note that the dashed white line in each figure indicates the location of the unperturbed interface obtained from companion simulations under the same shock conditions.

Immediately following the shock interaction, the perturbed interface undergoes a phase inversion due to the negative growth rate resulting from the $A < 0$ condition.[42] The growth from the first-shock interaction is shown in Figs. 4(b) and 4(c), while Fig. 4(c) also shows the arrival of the second shock at a scaled time $(t - t_{SI2})/\tau^{++} = 0$. Following the second-shock interaction, a second phase inversion is observed in Fig. 4(d) corresponding to a nondimensional time of ~2.2. The subsequent nonlinear growth and saturation of bubbles are summarized in Figs. 4(e)–4(g). At late times, bubbles converge to a rounded tip, while spikes are narrow and pointed and appear to grow indefinitely with a terminal velocity. In our simulations, the bubble velocities decay asymptotically as ~$1/t$, in agreement with hydrodynamic models, while experiments suggest bubble growth is arrested at a finite amplitude, possibly owing to other physics not included here. Relatedly, in the simulations that correspond to idealized conditions, the spike jets do not suffer a break up at late times, since surface tension effects were not included. In spite of these late-time differences with experimental observations, such simulations are valuable since they provide a reliable description of the underlying hydrodynamic aspects that determine gross aspects of bubble and spike growth, including their velocities. Furthermore, as reviewed in Sec. II (and elsewhere in Refs. 7 and 16), models for bubble/spike velocities and source models for ejecta mass are based on purely hydrodynamic potential flow theory.[10] The simulations summarized in this paper and in Refs. 7 and 16 can thus be directly compared with the results of such models.

The density contours in Fig. 5 correspond to case 5, which had a scaled initial amplitude $kh_0^- = 0.5$ [Fig. 5(a)], while the bubbles were allowed to mature to a scaled amplitude $kh_{bu}^{--} = 1.3$ before second-shock impact [Fig. 5(c)]. Since the bubbles had evolved over ~6.8τ^{++} before reshock, additional features due to secondary instabilities are visible in Fig. 5(c). Following the second-shock impact, the bubble shape inverts and the secondary features are amplified from the baroclinic vorticity

TABLE I. Summary of double-shock numerical simulations, with corresponding interface properties for first and second shocks.

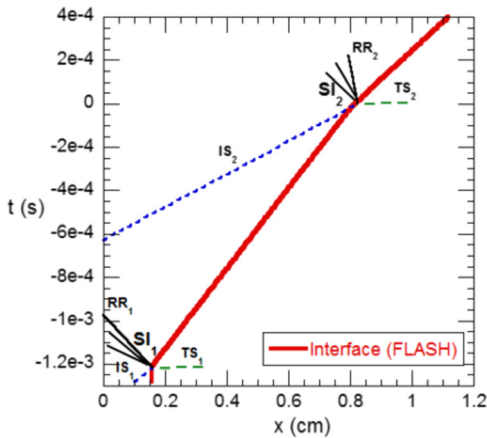| Case	Initial shape	Scaled initial amplitude kh_0^-	Scaled bubble amplitude before second shock kh_{bu}^{--}	Bubble half-width before second shock L_{bu}^{--} (cm)	Chord length b (cm)	Bubble wavelength λ_{eff} (cm)
1	Sine	0.12	0.45	0.300	0.412	1.13
2	Sine	0.12	0.75	0.335	0.443	1.25
3	Sine	0.12	0.96	0.336	0.423	1.24
4	Sine	0.12	0.5	0.300	0.411	1.12
5	Sine	0.5	1.32	0.380	0.448	1.38
6	Chevron	0.5	1.38	0.385	0.447	1.40

FIG. 3. Typical x–t diagram for double-shock simulations. IS, incident shock; TS, transmitted shock; RR, reflected rarefaction; SI, shock–interface interaction. Subscripts indicate first or second shock.

deposited at the interface into the smaller spikes located at $y = \lambda/2$ and $3\lambda/2$. In spite of the appearance of secondary instabilities, the dominant features eventually establish themselves, as observed in Figs. 5(a)–5(c). Similar to case 1, these features include a concave bubble tip and a narrow spike jet whose shape is determined by the influence of higher

harmonics. Finally, qualitative results from the chevron case are presented in Figs. 6(a)–6(e). The interface properties at first and second shock were $kh_0^- = 0.5$ and $kh_{bu}^{--} = 1.3$, since the bubble evolved to $\tau^{++} \sim 7$, at which time they were reshocked. While the interface shapes immediately following the first and second shocks are different owing to the presence of higher harmonics in the Fourier series representation, these effects subside quickly, leaving the primary mode to dominate at late times in a manner similar to cases 1 and 5 [the amplitude of the nth term in the Fourier series decays as $\sim(2n+1)^{-2}$, as shown in Ref. 7]. Note that the chevron perturbation has the same missing area as a sinusoid of the same wavelength, given by $A_{sh} = h_0\lambda$, so that $\lambda_{eff} = \lambda$.

From images such as those in Figs. 4–6, we infer the amplitudes of bubbles and spikes using the following approach. The bubble tip position x_{bu} is defined as the x location where the planar-averaged (y) density dropped below 90% of the release density of the liquid metal. Similarly, the spike position x_{sp} is identified as the x location where the planar-averaged (y) mass fraction of the heavy fluid dropped below 1%. The location of the free surface x_{fs} is obtained by requiring that

$$m(t) = \int_{x_{bu}(t)}^{x_{fs}(t)} [\rho_{rel} - \langle\rho(x)\rangle]\, dx = \int_{x_{fs}(t)}^{\infty} \langle\rho(x)\rangle\, dx, \quad (17)$$

Eq. (17) is solved iteratively for $x_{fs}(t)$, which is then used to calculate the bubble and spike amplitudes according to $h_{bu/sp} = |x_{bu/sp} - x_{fs}|$. We plot these quantities and corresponding velocities for cases 1, 5, and 6 in Figs. 7–9, respectively.
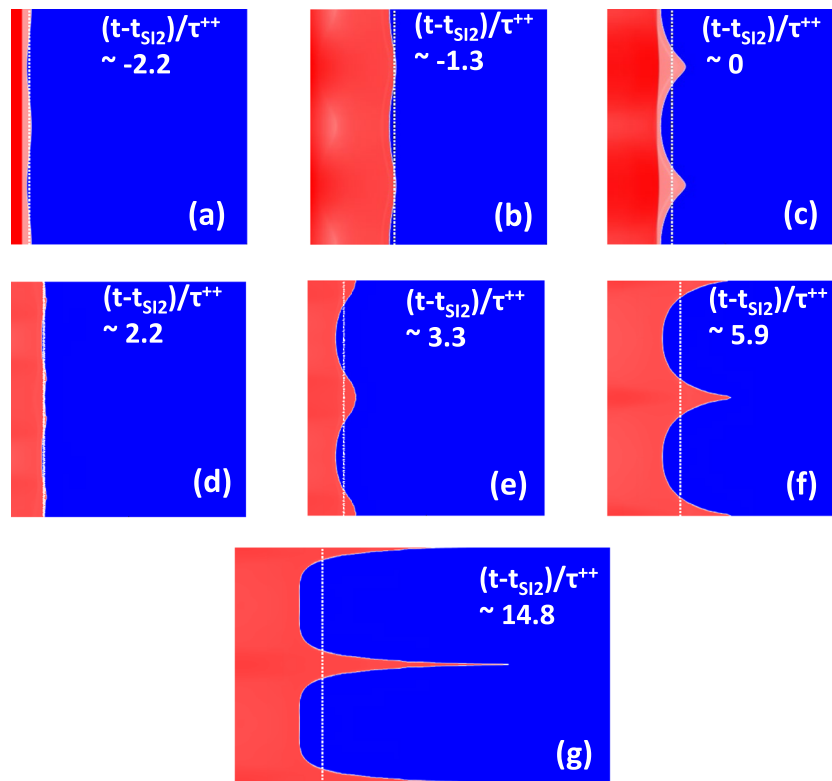

FIG. 4. Density contours from numerical simulations of case 1 with sinusoidal initial perturbation ($kh_{bu}^{--} \sim 0.45$ at the second shock).
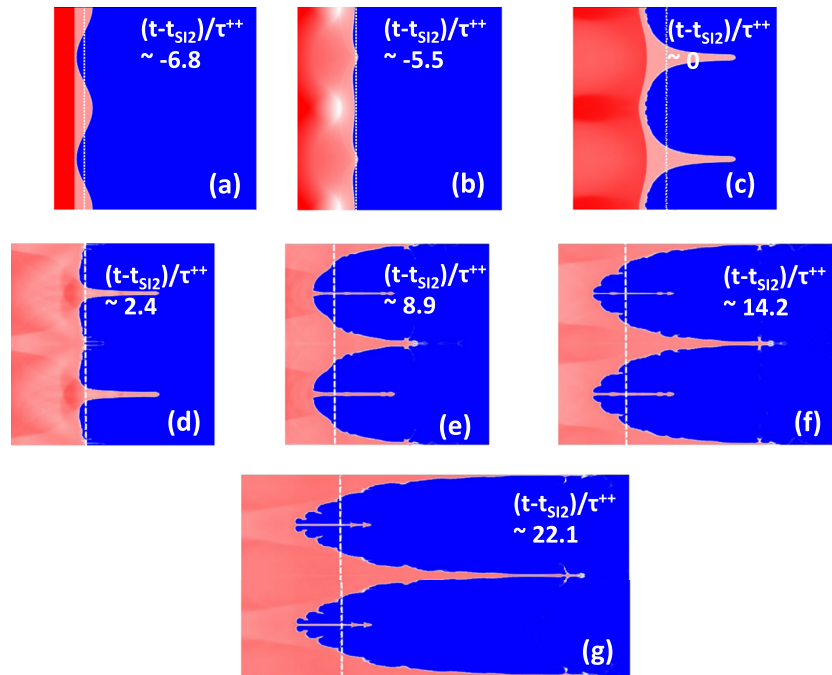
FIG. 5. Density contours from numerical simulations of case 5 with sinusoidal initial perturbation ($kh_{bu}^{--} \sim 1.32$ at the second shock).

Figures 7(a) and 7(b) show the evolution of the scaled bubble and spike amplitudes kh_{bu} and kh_{sp} as functions of the nondimensional time. We take the initial bubble (spike) amplitudes as positive (negative) in sign, so that the second-shock interaction leads to sign reversals in these quantities. The bubble amplitude kh_{bu}^{++} in Fig. 7(a) shows a saturation-like behavior for large values of $(t - t_{SI2})/\tau^{++}$. As can be seen in Fig. 7(b), spike amplitudes grow linearly and without bound in the absence of mitigating factors such as material strength.
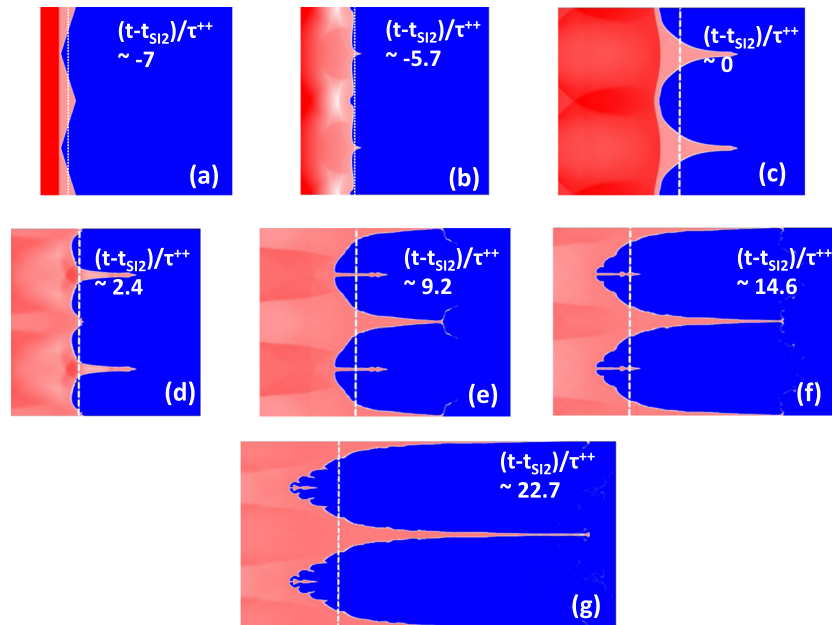

FIG. 6. Density contours from numerical simulations of case 6 with chevron initial perturbation ($kh_{bu}^{--} \sim 1.38$ at the second shock).
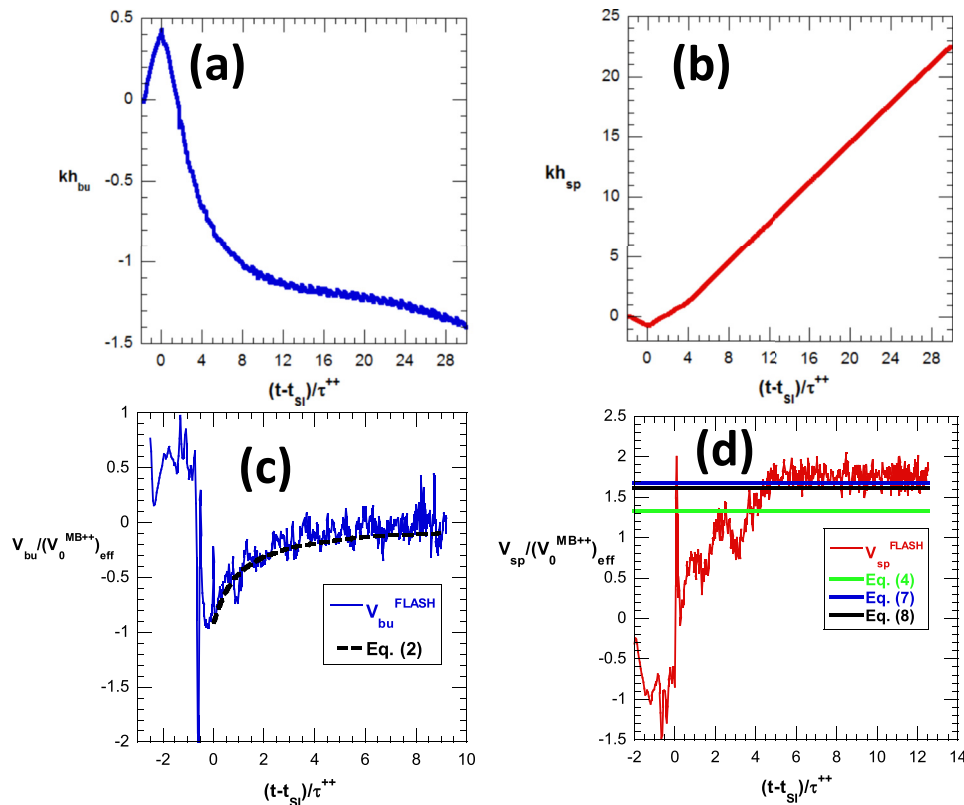
FIG. 7. Scaled plots of (a) bubble amplitude, (b) spike amplitude, (c) bubble velocity, and (d) spike velocity vs nondimensional time for case 1, and comparison with models.

The bubble and spike velocities plotted in Figs. 7(c) and 7(d) are scaled with the ideal linear growth rate from Eq. (1), which has been evaluated here for second-shock conditions and using λ_{eff} obtained from fitting the second-shock bubble surface to a flycut using the procedure described in Sec. II B. When the potential flow model of Ref. 10 given in Eq. (2) is evaluated using λ_{eff}, it is in excellent agreement with the scaled bubble velocities from our FLASH simulations.

The corresponding scaled spike velocities are shown in Fig. 7(d), and it can be seen that an asymptotic velocity is achieved following a brief rise time. We compare our simulation results for the spike velocity with the potential flow model of Ref. 36 as well as the empirical models of Ref. 16 and Eq. (8). Once again, all models were evaluated using λ_{eff} computed from a flycut fit to the bubble surface at the instant of the second shock. The empirical model of Ref. 16 was evaluated using ϕ_{sp} corresponding to $\gamma_A = 3$, to match the ideal gas representation of the shocked liquid metal in our simulations. The empirical models are in excellent agreement with the simulations, while the incompressible potential flow model of Ref. 36 slightly under-predicts the late-time velocities owing to the finite values of $M_i kh_0^-$ at the second shock.

Figure 8 plots amplitudes and velocities from case 5, where the bubble had evolved to $kh_{bu}^- = 1.3$ at second-shock impact. The results from this case follow the same trends as the lower-amplitude data presented in Fig. 7, although the presence of secondary instabilities

shown in Fig. 5 introduces some transient aspects in the spike behavior. As the bubble initial amplitude kh_{bu}^- was larger in this case, the time to nonlinear saturation, t_{nl}/τ, increases, as observed in Fig. 8(a). When evaluated with the effective wavelength λ_{eff} for a fitted flycut surface, the potential flow model of Ref. 10 gives excellent agreement with the simulation data [Fig. 8(c)]. Spike velocities from this case are shown in Fig. 8(d), and exhibit prolonged transients following the second-shock event, owing to the presence of secondary instabilities discussed earlier. Since the secondary spikes [Figs. 5(e)–5(g)] occur at a smaller scale (higher k_{eff}), a period of higher growth rates is observed at first [for $0 \le (t - t_{SI2})/\tau^{++} \le 10$], as expected from Eq. (1). Eventually [at $(t - t_{SI2})/\tau^{++} > 10$], the secondary structures are dominated by the fundamental mode, and the observed nonlinear velocity saturates to a constant value that agrees with the empirical models [Eqs. (7) and (8)] when evaluated using the procedure discussed in Sec. II. Once again, the incompressible potential flow model of Ref. 36 slightly under-predicts the observed spike velocities, owing to the finite values of $M_i kh_0^-$ for this case. The corresponding results for case 6 with a chevron initial perturbation are shown in Figs. 9(a)–9(d). For both first and second shocks, case 6 had bubble initial conditions similar to case 5. As a result, the developments of bubble and spike amplitudes and velocities show similar behavior to the sinusoidally perturbed case 5.

We summarize bubble and spike velocities from all the simulations listed in Table I in Figs. 10(a) and 10(b). For bubbles, the
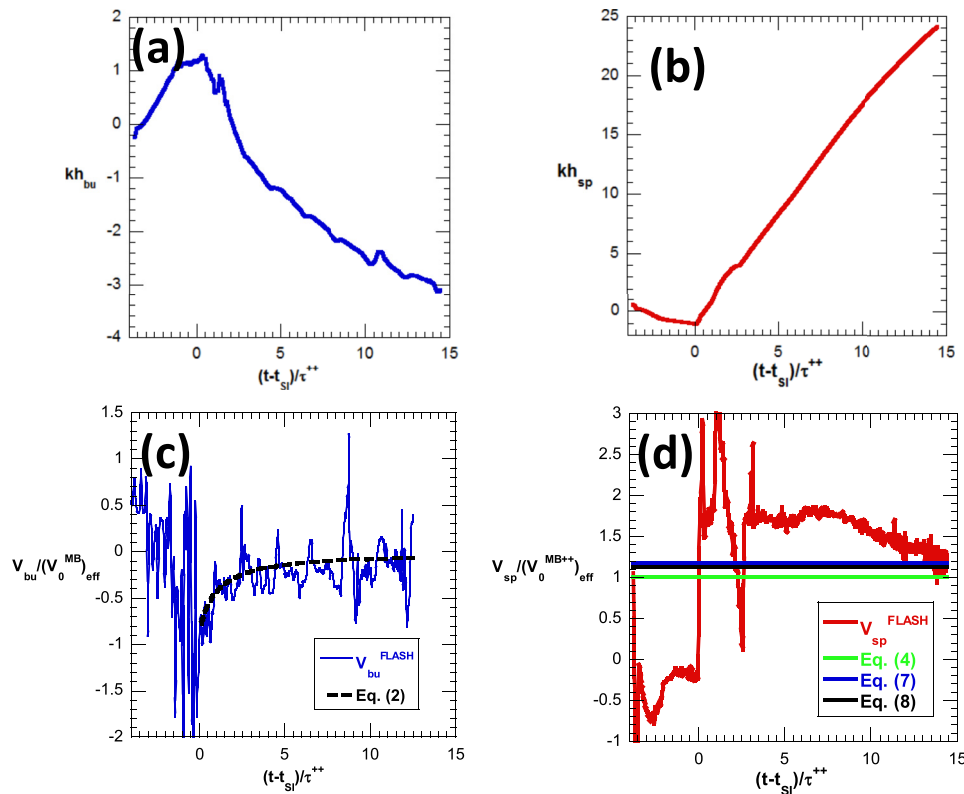
FIG. 8. Scaled plots of (a) bubble amplitude, (b) spike amplitude, (c) bubble velocity, and (d) spike velocity vs nondimensional time for case 5, and comparison with models.

velocities are scaled with the potential flow model [Eq. (2)] evaluated with k_{eff}. Figure 10(a) shows that the scaling collapses bubble velocities from cases 1–6, and in agreement with Eq. (2). Similarly, we scale spike velocities with Eq. (8) using k_{eff}, leading to a collapse of all the data, in agreement with the proposed empirical model. As noted earlier, the short-term transients due to secondary instabilities do not follow this scaling, but these effects subside as the dominant mode asserts itself at late times. The dependence of the asymptotic spike velocities from the second shock on the scaled bubble amplitude $k_{eff}h_0$ is shown in Fig. 11. The velocities from the FLASH simulations and models are scaled with the impulsive model prediction from Eq. (1). We find that over the range of double-shock conditions investigated here ($M_i k h_0^{--} \gg 1$), our empirical model is in very good agreement with simulation data. We also plot in Fig. 11 the terminal spike velocity at the end of the first shock ($k_{eff}h_0 = 0.12$), which is predicted accurately by our empirical model [Eq. (8)]. In contrast, the empirical model of Ref. 16 over-predicts the first-shock data owing to the choice of the parameter ϕ_{sp} in Eq. (7).

B. Analysis of experimental data

In this section, we provide a possible approach to analyze experimental data from doubly shocked ejecta. A significant challenge in high-strain-rate experiments is that the interface properties immediately preceding the second shock are not available from measurements. We suggest a method to evaluate our empirical model

for experimental conditions when the interface shape, particularly the bubble surface length L_{bu}^{--}, is not directly available. We then compare the model predictions with the recent double-shocked experimental campaign[24,25] conducted at LANL.

We briefly review the experimental configuration used in Refs. 24 and 25, and refer the reader to those articles for additional details. The experiments described there were based on a two-shockwave tool developed at LANL, in which a machined Sn target is driven by explosive loading from a HE PBX 9501 package coupled to TNT. The detonation constitutes the first shock incident on the target, while a reflected wave bounces off a back anvil to form the second shock. Diagnostics fielded in the experiments included lithium niobate (LN) piezoelectric probes that convert measured pressure signals from ejecta impact on the probe surface to mass measurements using a time-of-flight technique.[24] Laser Doppler velocimetry (LDV) probes were also used, and provide time-resolved line-of-sight velocity measurements associated with the ejecta, free surface, and receding bubble. The physics package included a circular Sn coupon, with machined grooves corresponding to a dominant wavelength $\lambda \sim 80\,\mu$m and half-amplitude $h_0 \sim 1.5\,\mu$m, with $kh_0^- \sim 0.12$ for the first shock. The experiments reported in Refs. 24 and 25 were at three different initial shock pressures, and in the following we discuss the two shots with the highest pressures, 24.5 GPa and 26.4 GPa, which were labeled shots 1755 and 1756, respectively. The third shot was conducted at 18.5 GPa, below the melt line for Sn, so the ejecta would have been in a solid state.[24]
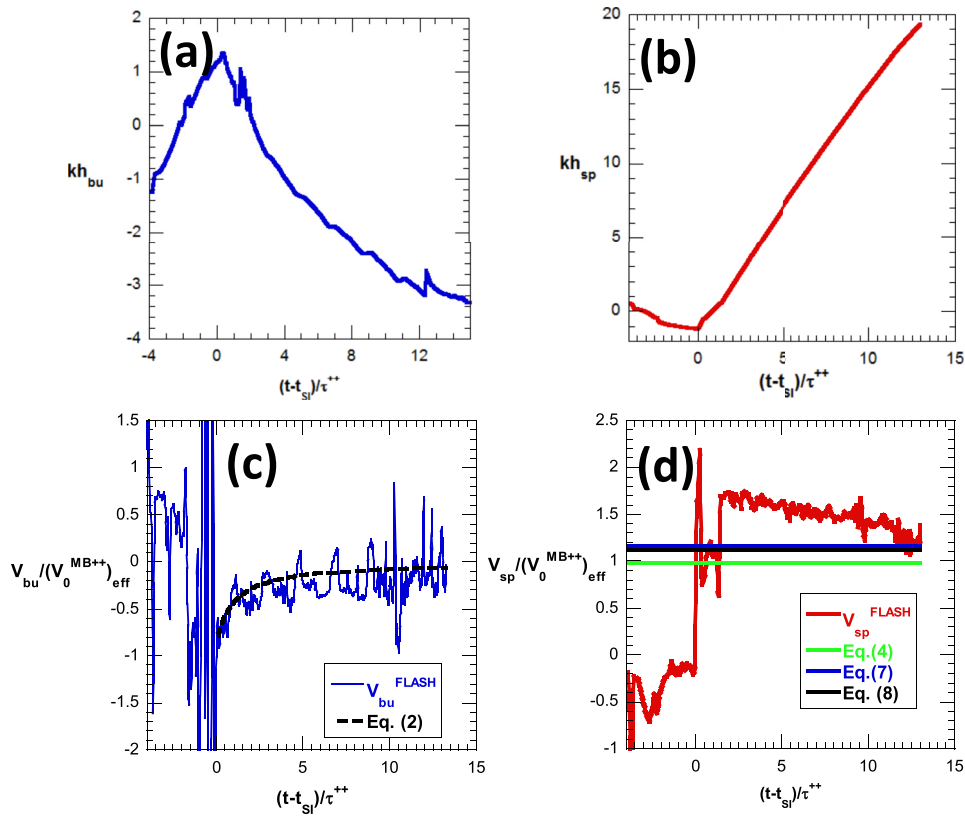
FIG. 9. Scaled plots of (a) bubble amplitude, (b) spike amplitude, (c) bubble velocity, and (d) spike velocity vs nondimensional time for case 6, and comparison with models.

As discussed earlier, our approach for evaluating the effective wavelength of the mature bubble surface involves fitting the shape to a flycut profile using the independent parameters $(h_{bu}^{--}, L_{bu}^{--}, \lambda)$. Owing to the high strain rates and limited optical access in experiments, the pre-second-shock bubble amplitude and lateral length scale are typically not available. This is further complicated by the speculation[24] that the recompaction from the second shock causes some of the first-shock ejecta to detach from the bulk, leaving behind a truncated interface of unknown amplitude. Given these uncertainties in the interface profile, we adopt the following two-step approach to
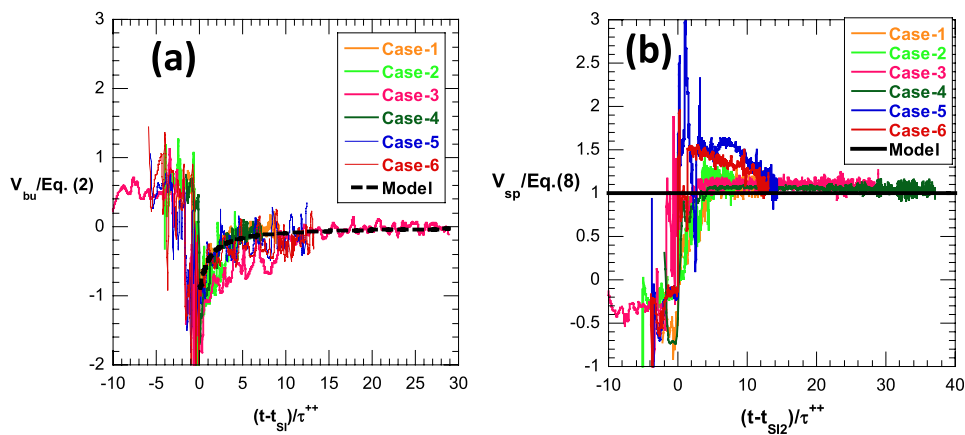

FIG. 10. (a) Bubble velocities from all simulations scaled with the model of Ref. 10. (b) Spike velocities from all simulations scaled with Eq. (8).
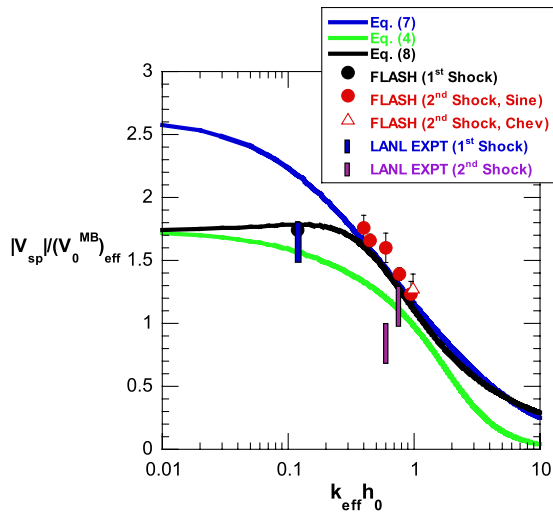
FIG. 11. Summary plot: comparison of spike velocities from all models with FLASH data for single-shock and double-shock cases, as well as reported growth rates from experiments.[24,25]

determine h_{bu}^{--} and L_{bu}^{--} for evaluating the amplitude and the effective wavelength of the equivalent flycut.

1. Determination of bubble amplitude h_{bu}^{--}

The saturated bubble amplitude may be determined from the cumulative ejecta mass reported by the LN probes at the end of the experiments. The cumulative mass from the second shock is sourced by the bubble before second-shock arrival. Note that, in contrast to our numerical simulations, this assumes the bubbles in the experiment arising from the first shock eventually saturate to a finite amplitude and form the initial conditions for the second shock. This is a reasonable assumption, since the experiments are run to very late times kV_0t, and the bubble motion is likely hindered by viscous and other effects. The ejecta mass (from the second shock) may then be related to the saturated bubble (from the first shock) initial conditions using the model of Ref. 16:

$$\sigma_{ejecta}^{++} = \rho_A^{++} \left| h_{bu}^{--} \right|, \tag{18}$$

where σ_{ejecta}^{++} is the measured ejecta areal density from second shock in the experiments, and ρ_A^{++} is the post-second-shock density of Sn and can be determined from Table IV in Ref. 16 for a given incident shock pressure. Using Eq. (18) and reported values of σ_{ejecta}^{++} measured in the experiments, we obtain the pre-second-shock bubble amplitudes for shots 1755 and 1756 as $h_{bu}^{--} \sim 5.6$ and 8.4 μm, respectively.

2. Determination of bubble half-width L_{bu}^{--}

To determine the bubble half-width L_{bu}^{--}, we assume that the bubbles have evolved self-similarly, and compute the limiting streamlines from the self-similar potential flow model of Ref. 11 to determine the intercept with the free surface. The equation for the streamlines in a bubble-attached coordinate system (x', y') is[11]

$$\frac{dy'}{dx'} = \frac{-\arctan\left(\frac{\sin y'}{\cos y' + e^{-x'}}\right)}{\frac{a}{b} + \frac{1}{2}\ln\left(1 + 2e^{x'}\cos y' + e^{2x'}\right)}, \tag{19}$$

where a and b are dimensionless coefficients that must satisfy the flow boundary conditions. Equation (19) was derived in Ref. 11 in self-similar coordinates in which the bubble tip is fixed at $-x'_a$, while the spike tip is at $+\infty$. It can be used to compute the limiting streamline that skirts the bubble surface [originating from $(-\infty, \pi)$], following which the solution is transformed back to the laboratory coordinates (x, y) using the mapping[11]

$$x \rightarrow \frac{\lambda}{2\pi}\left[x' - a\ln\left(\frac{t}{\tau^+}\right)\right],$$
$$y \rightarrow \frac{\lambda}{2\pi}y'. \tag{20}$$

Thus, we determine the bubble width as the intercept of the limiting streamline with the free surface (located at $x = 0$). The missing area is then computed using Eq. (15) for a flycut, and we obtain $A_{shape} = 328$ μm^2 and 587 μm^2 for shots 1755 and 1756, respectively. The corresponding effective wavelengths of the saturated bubble are 58 μm ($k_{eff}h_{bu}^{--} \sim 0.6$) and 70 μm ($k_{eff}h_{bu}^{--} \sim 0.75$) for shots 1755 and 1756, respectively. Finally, we also determine the bubble effective wavelength by directly integrating for the area under the limiting streamlines and obtain $A_{shape} = 329$ μm^2 and 591 μm^2 for the above cases. This confirms that the flycut shape approximation recommended here accurately captures the properties of the bubble, in agreement with the self-similar, potential flow theory.

In Fig. 11, we compare the predictions from different models (based on the above estimation of $k_{eff}h_{bu}^{--}$) with ejecta velocity data from LDV pins in the LANL experiments.[24,25] Since there is some variation in the data between the pins for a given experiment, the experimental data points in Fig. 11 are plotted as rectangular symbols with the vertical extent spanning the range of reported values. As expected, the best agreement with the hydrodynamic models is observed for shot 1756, which had the highest shock pressures, ensuring the ejecta were in a molten state. For this case, all three models provide good agreement with data. The growth rates from shot 1755 were likely compromised by material strength effects, since the ejecta were likely in a mixed state. For these conditions, all the hydrodynamic models over predict the experimental data point. We also show in Fig. 11 the asymptotic ejecta velocities from the first shock from the LDV readout ($kh_0^- = 0.12$). This data point straddles the prediction curves from our empirical model and the potential flow model of Ref. 36. Owing to the lower values of kh_0^- for the first shock, the empirical model of Ref. 16 over-predicts the experimental data.

V. SUMMARY

We have proposed an approach for predicting ejecta velocities from metallic surfaces when they are driven by multiple shocks in sequence. The procedure is validated for the special case of two shocks, assuming each shock is strong enough to melt the material (on shock or on release[23]). Our central hypothesis is the bubble cavity immediately prior to the second shock forms the initial conditions for the subsequent ejecta formation and is responsible for sourcing the ejecta mass. If the bubble has already reached a nonlinear state, then the initial conditions correspond to a nonsinusoidal surface. We find that a flycut

approximation best describes the bubble shape at such late times. Our prescription for describing the subsequent dynamics is to use an effective wavelength λ_{eff} of such a flycut profile to describe the bubble shape in the models for bubble and spike velocities as well as ejecta mass. The approach has been validated for ejecta mass previously,[31] and we have shown the applicability of this method to velocities in this paper.

Thus, our suggestion is to treat the pre-second-shock bubble initial condition as a flycut surface and compute the corresponding λ_{eff} for use in the velocity models. For bubbles, the potential flow theory of Ref. 10 has been evaluated using this strategy. For spikes, we have tested three contending models and have found that our empirical model provides good agreement with data, since it accounts for both nonlinearities as well as compressibility through the shock Mach number. A key aspect of our model is the recognition that these two effects act in concert through the $M_i k h_0$ term, so that, even at moderate shock Mach numbers, the growth rates can be affected if the initial amplitudes are nonlinear. This is certainly the case in experiments, which are often initialized with finite amplitudes, and especially true in double-shock experiments where the bubble has been allowed to develop to a fairly mature state before being reshocked. The incompressible, potential flow model of Ref. 36 is exact and has been included in our comparison to highlight the significance of the combined $M_i k h_0$ term even at low values of M_i. The proposed model contains no tunable coefficients and computes ejecta velocities without requiring information on the initial growth rate V_{sp0}, which can be ambiguous. We have tested these ideas by comparison with continuum numerical simulations using the FLASH code, for different initial amplitudes and shapes at the second shock. For all the cases studied here, our empirical model given by Eq. (8) provides the best agreement with data when combined with the approach described above.

We have also provided an approach for analyzing experimental data where there is often significant uncertainty in determining the interface properties before the second shock. To compute the effective wavelength, we suggest using a self-similar model such as that of Ref. 11 and determining the bubble width L_{bu}^{--} as the intercept of the calculated streamlines with the free surface. To constrain the bubble tip location, the bubble amplitude is estimated from the measured cumulative ejecta mass using a source model[16] that assumes a saturated bubble at late times. The approach appears promising, and, for the experiments where the shock pressure exceeded the melt condition, the measured velocities are in agreement with models evaluated using this approach. However, the comparison with experiments provided here is preliminary, and a broader examination of experimental data is required. We close by noting that the models and approaches presented here will be of value in interpreting such experimental campaigns involving shocked targets.

ACKNOWLEDGMENTS

REFERENCES

[1] J. D. Lindl, *Inertial Confinement Fusion: The Quest for Ignition and Energy Gain Using Indirect Drive* (Springer, New York, 1998).

[2] M. Zingale, S. E. Woosley, C. A. Rendleman, M. S. Day, and J. B. Bell, "Three-dimensional numerical simulations of Rayleigh-Taylor unstable flames in type 1a supernovae," Astrophys. J. **632**(2), 1021 (2005).

[3] M. Herant, W. Benz, W. R. Hix, C. L. Fryer, and S. A. Colgate, "Inside the supernova: A powerful convective engine," Astrophys. J. **435**, 339 (1994).

[4] C.-Y. Wang and R. A. Chevalier, "Instabilities and clumping in type Ia supernova remnants," Astrophys. J. **549**(2), 1119 (2001).

[5] R. D. Richtmyer, "Taylor instability in shock acceleration of compressible fluids," Commun. Pure Appl. Math. **13**, 297 (1960).

[6] E. E. Meshkov, "Instability of the interface of two gases accelerated by a shock," Fluid Dyn. **4**, 101 (1969).

[7] F. J. Cherne, J. E. Hammerberg, M. J. Andrews, V. Karkhanis, and P. Ramaprabhu, "On shock driven jetting of liquid from non-sinusoidal surfaces into a vacuum," J. Appl. Phys. **118**, 185901 (2015).

[8] A. B. Georgievskaya and V. A. Raevsky, "A model of a source of shock wave metal ejection based on Richtmyer–Meshkov instability theory," J. Dyn. Behav. Mater. **3**, 321 (2017).

[9] J. E. Hammerberg, W. T. Buttler, F. J. Cherne, M. J. Andrews, V. Karkhanis, P. Ramaprabhu, G. D. Stevens, and W. D. Turley, "A source model for ejecta," J. Dyn. Behav. Mater. **3**, 316 (2017).

[10] K. O. Mikaelian, "Analytic approach to nonlinear Rayleigh-Taylor and Richtmyer-Meshkov instabilities," Phys. Rev. Lett. **80**, 508 (1998).

[11] R. J. R. Williams, "The late time structure of high density contrast, single mode Richtmyer-Meshkov flow," Phys. Fluids **28**, 074108 (2016).

[12] J. E. Hammerberg et al., "Proton radiography measurements and models of ejecta structure in shocked Sn," AIP Conf. Proc. **1979**, 080006 (2018).

[13] G. Dimonte, G. Terrones, F. J. Cherne, T. C. Germann, V. Dupont, K. Kadau, W. T. Buttler, D. M. Oro, C. Morris, and D. L. Preston, "Use of the Richtmyer-Meshkov instability to infer yield stress at high-energy densities," Phys. Rev. Lett. **107**, 264502 (2011).

[14] M. B. Prime, W. T. Buttler, M. A. Buechler, N. A. Denissen, M. A. Kenamond, F. G. Mariam, J. I. Martinez, D. M. Oro, D. W. Schmidt, J. B. Stone, D. Tupa, and W. Vogan-McNeil, "Estimation of metal strength at very high rates using free-surface Richtmyer–Meshkov instabilities," J. Dyn. Behav. Mater. **3**, 189 (2017).

[15] J. R. Asay, "Material ejection from shock-loaded free surfaces of aluminum and lead," Report No. SAND-76-0542, 1976.

[16] G. Dimonte, G. Terrones, F. J. Cherne, and P. Ramaprabhu, "Ejecta source model based on the nonlinear Richtmyer-Meshkov instability," J. Appl. Phys. **113**, 024905 (2013).

[17] O. Durand and L. Soulard, "Large-scale molecular dynamics study of jet breakup and ejecta production from shock-loaded copper with a hybrid method," J. Appl. Phys. **111**, 044901 (2012).

[18] O. Durand and L. Soulard, "Power law and exponential ejecta size distributions from the dynamic fragmentation of shock-loaded Cu and Sn metals under melt conditions," J. Appl. Phys. **114**, 194902 (2013).

[19] R. J. R. Williams and C. C. Grapes, "Simulation of double-shock ejecta production," J. Dyn. Behav. Mater. **3**, 291 (2017).

[20] G. Ren, Y. Chen, T. Tang, and Q. Li, "Ejecta production from shocked Pb surface via molecular dynamics," J. Appl. Phys. **116**, 133507 (2014).

[21] J.-L. Shao, P. Wang, A.-M. He, S.-Q. Duan, and C.-S. Qin, "Atomistic simulations of shock-induced microjet from a grooved aluminium surface," J. Appl. Phys. **113**, 153501 (2013).

[22] A.-M. He, J. Liu, C. Liu, and P. Wang, "Numerical and theoretical investigation of jet formation in elastic-plastic solids," J. Appl. Phys. **124**, 185902 (2018).

[23] W. T. Buttler, D. M. Oro, D. L. Preston, K. O. MIkaelian, F. J. Cherne, R. S. Hixson, F. G. Mariam, C. Morris, J. B. Stone, G. Terrones, and D. Tupa, "Unstable Richtmyer–Meshkov growth of solid and liquid metals in vacuum," J. Fluid Mech. **703**, 60 (2012).

[24] W. T. Buttler, D. M. Oro, R. T. Olson, F. J. Cherne, J. E. Hammerberg, R. S. Hixson, S. K. Monfared, C. L. Pack, P. A. Rigg, J. B. Stone, and G. Terrones, "Second shock ejecta measurements with an explosively driven two-shockwave drive," J. Appl. Phys. **116**(10), 103519 (2014).

[25] W. T. Buttler, D. M. Oro, F. G. Mariam, A. Saunders, M. J. Andrews, F. J. Cherne, J. E. Hammerberg, R. S. Hixson, S. K. Monfared, C. Morris, R. T. Olson, D. L. Preston, J. B. Stone, G. Terrones, D. Tupa, and W. Vogan-McNeil, "Explosively

driven two-shockwave tools with applications," J. Phys.: Conf. Ser. **500**(11), 112014 (2014).

[26]R. Cheret, P. Chapron, P. Elias, and J. Martineau, "Mass ejection from the free surface of shock-loaded metallic samples," in *Shock Wave in Condensed Matter, 1985*, edited by Y. M. Gupta (Plenum, New York, 1986), p. 651.

[27]V. Frachet, P. Elias, and J. Martineau, "Matter ejection from shocked material: A physical model to understand the effects of free surface defects," in *Shock Wave in Condensed Matter, 1987*, edited by S. C. Schmidt and N. C. Holmes (Elsevier Science, 1988), p. 235.

[28]W. T. Buttler, R. J. R. Williams, and F. M. Najjar, "Foreword to the special issue on ejecta," J. Dyn. Behav. Mater. **3**, 151 (2017).

[29]R. J. R. Williams, "Ejecta sources and scalings," AIP Conf. Proc. **1979**, 080015 (2018).

[30]A. A. Charakhch'an, "Richtmyer–Meshkov instability of an interface between two media due to passage of two successive shocks," J. Appl. Mech. Tech. Phys **41**(1), 23 (2000).

[31]V. Karkhanis, P. Ramaprabhu, W. T. Buttler, J. E. Hammerberg, F. J. Cherne, and M. J. Andrews, "Ejecta production from second shock: Numerical simulations and experiments," J. Dyn. Behav. Mater. **3**(2), 265 (2017).

[32]V. Karkhanis, P. Ramaprabhu, F. J. Cherne, J. E. Hammerberg, and M. J. Andrews, "A numerical study of bubble and spike velocities in shock-driven liquid metals," J. Appl. Phys. **123**, 025902 (2018).

[33]K. A. Meyer and P. J. Blewett, "Numerical investigation of the stability of a shock-accelerated interface between two fluids," Phys. Fluids **15**, 753 (1972).

[34]D. Layzer, "On the instability of superposed fluids in a gravitational field," Astrophys. J. **122**, 1 (1955).

[35]A. L. Velikovich and G. Dimonte, "Nonlinear perturbation theory of the incompressible Richtmyer-Meshkov instability," Phys. Rev. Lett. **76**, 3112 (1996).

[36]Q. Zhang, "Analytic solutions of Layzer-type approach to unstable interfacial fluid mixing," Phys. Rev. Lett. **81**, 3391 (1998).

[37]G. Dimonte and P. Ramaprabhu, "Simulations and model of the nonlinear Richtmyer–Meshkov instability," Phys. Fluids **22**, 014104 (2010).

[38]B. Fryxell, K. Olson, P. Ricker, F. X. Timmes, M. Zingale, D. Q. Lamb, P. MacNeice, R. Rosner, J. W. Truran, and H. Tufo, "FLASH: An adaptive mesh hydrodynamics code for modeling astrophysical thermonuclear flashes," Astrophys. J., Suppl. Ser. **131**, 273 (2000).

[39]A. S. C. FLASH, University of Chicago, Chicago, 2005.

[40]P. Colella and P. R. Woodward, "The piecewise parabolic method (PPM) for gas-dynamical simulations," J. Comput. Phys. **54**, 174 (1984).

[41]K. O. Mikaelian, "Freeze-out and the effect of compressibility in the Richtmyer–Meshkov instability," Phys. Fluids **6**, 356 (1994).

[42]R. L. Holmes, G. Dimonte, B. Fryxell, M. L. Gittings, J. W. Grove, M. Schneider, D. H. Sharp, A. L. Velikovich, R. P. Weaver, and Q. Zhang, "Richtmyer–Meshkov instability growth: Experiment, simulation, and theory," J. Fluid Mech. **389**, 55 (1999).